International Journal of Minerals, Metallurgy and Materials
Volume 21, Number 7, July 2014, Page 666
DOI: 10.1007/s12613-014-0956-z

3D stress simulation and parameter design during twin-roll casting of 304 stainless steel based on the Anand model

Jing Guo[1)], *Yuan-yuan Liu*[2)], *Li-gang Liu*[1)], *Yue Zhang*[3)], *and Qing-xiang Yang*[1)]

1) State Key Laboratory of Metastable Materials Science & Technology, Yanshan University, Qinhuangdao 066004, China

2) Nanjing Iron & Steel Co., ltd., Nanjing 210035, China

3) School of Material Science and Engineering, University of Science and Technology Beijing, Beijing 100081, China

(Received: 12 December 2013; revised: 13 January 2014; accepted: 16 January 2014)

Abstract: This study first investigated cracks on the surface of an actual steel strip. Formulating the Anand model in ANSYS software, we then simulated the stress field in the molten pool of type 304 stainless steel during the twin-roll casting process. Parameters affecting the stress distribution in the molten pool were analyzed in detail and optimized. After twin-roll casting, a large number of transgranular and intergranular cracks resided on the surface of the thin steel strip, and followed a tortuous path. In the molten pool, stress was enhanced at the exit and at the roller contact positions. The stress at the exit decreased with increasing casting speed and pouring temperature. To ensure high quality of the fabricated strips, the casting speed and pouring temperature should be controlled above 0.7 m/s and 1520°C, respectively.

Keywords: stainless steel; strip metal; roll casting; stress; surface cracks; numerical analysis

1. Introduction

Twin-roll casting is a sustainable, environmentally friendly technology that is compatible with iron and steel recycling [1–4]. However, metal strips fabricated by the twin-roll strip casting process are prone to cracking. These cracks seriously degrade the mechanical properties of the strips, rendering them unsuitable for subsequent processing and application [5–6]. Cracking of the strip surface is associated with the stress state during solidification. Therefore, the stress in the thin steel strip during twin-roll casting is an important determiner of strip quality.

To date, most studies on thin steel strips manufactured by twin-roll casting have focused on the temperature field [7–8], thermal-flow coupling [9–12] and thermal-mechanical coupling [13–14]. Little attention has been paid to the internal stresses developed in the strip and molten pool [15–16].

Since few mechanical models of the twin-roll casting process have been published, simulations are based on numerous assumptions and are consequently imprecise. For instance, the mechanical behavior of thin steel strips is usually simulated by the elastic-plastic model, which neglects physical phenomena as the strip solidifies. To better model this behavior, new constitutive relations that reflect the physical phenomena during twin-roll casting should be established. Constitutive relationships have been extensively investigated, and a variety of constitutive models have been proposed. Among them, the unified Anand model is considered especially appropriate for many situations [17–18]. Hu and Ju [19] reported that the Anand model is suitable for analyzing molten pools and large deformation stresses. Therefore, in this work, we apply the Anand model to the stress field in a 3D molten steel pool, and find the optimal parameters that minimize cracking. Using the simulated results to guide the actual production, the twin-roll casting process could be easily and adequately controlled to yield high-quality products.

2. Experimental

The twin-roll casting machine comprises two rollers, filled with cooling water, that rotate in opposite directions

Corresponding author: Qing-xiang Yang E-mail: qxyang@ysu.edu.cn

with the same angular velocity, and side dams on both sides. The molten steel is first injected into the space between the two rollers and side dams to form a molten pool, and is eventually solidified into a casting strip by cooling under roller contact. A schematic of the twin-roll casting process is shown in Fig. 1(a). In this work, type 304 stainless steel strips of 2.0 mm in thickness were cast in a copper twin-rolling apparatus. The chemical composition of 304 stainless steel is listed in Table 1.

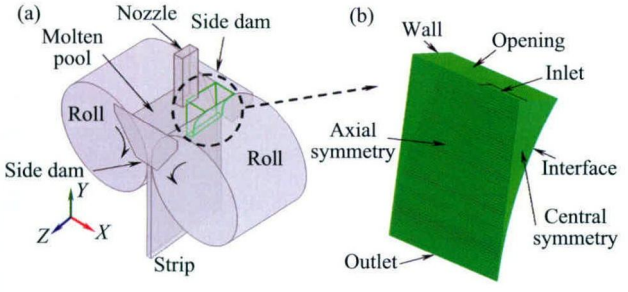

Fig. 1. Schematics of the twin roll casting process (a) and 1/4 finite element model of the molten pool (b).

Table 1. Chemical composition of AISI 304 stainless steel

wt%

C	Si	Mn	P	S	Cr	Ni	Mo
0.06	0.7	1.2	0.03	0.014	18	8	0.18

Cracks were visible on the surfaces of the stainless steel strips fabricated by twin-roll casting. Samples were excised from the cracked regions and etched by aqua regia (HNO_3 + 3HCL) for approximately 2 min. The etched samples were observed under an Axiovert 200 MAT optical microscope (OM) and an S4800–II field emission scanning electron microscope (FESEM) with energy dispersive spectroscopy (EDS).

To obtain sensible parameters for modeling, the specimens were machined into ϕ10 mm × 15 mm cylinders and hot compressive experiments were conducted in a Gleeble–3500 thermo-simulation machine (Dynamic Systems Inc. (DSI) in USA). In the real twin-roll casting process, the molten steel is rolled into a sheet within a short time, before the steel can appreciably cool. Consequently, the selected deformation temperatures were 1100, 1150, 1200 and 1250°C. During injection into the molten pool, the liquid steel is subjected to slight deformation under a small extrusion force. However, at the exit, where the extrusion force is much higher, the steel strip is severely deformed. To capture this wide range, the strain rates in the hot compressive experiments were varied over five orders of magnitude (0.001, 0.01, 0.1, 1, and 10 s^{-1}) with a maximum deformation of 50%. The stress–strain curves under different temperatures and strain rates were recorded by computer.

3. Simulation methods

3.1. Establishment of FE model

The sizes of the manufactured products were retained in the geometrical models. Since the pool is symmetric in the length and width directions, it was represented by a quarter of the real molten pool. Simulations were conducted in the professional software ANSYS ICEM CFD. The hexahedral grids of the model were meshed with 22740 elements and 20614 nodes. The finite element model of the molten pool and mesh generation are shown in Fig. 1(b). On this grid, the stress distribution of the molten pool under different casting speeds (0.3, 0.5, 0.7, 1.0 mm/s) and pouring temperatures (1480, 1500, 1520, and 1540°C) were simulated by ANSYS software.

The material parameters of 304 stainless steel strips are shown in Table 2. Here, ρ, M, c, η, and λ denote the density, molar mass, specific heat, dynamic viscosity and thermal conductivity, respectively.

Table 2. Material parameters of AISI 304 stainless steel

ρ / ($kg \cdot m^{-3}$)	M / ($g \cdot mol^{-1}$)	c / ($J \cdot kg^{-1} \cdot K^{-1}$)	η / ($kg \cdot m^{-1} \cdot s^{-1}$)	λ / ($W \cdot m^{-1} \cdot K^{-1}$)
7060	55.2	809.27	0.00685	33.51

Before simulating the stress field, the temperature field, previously obtained by thermal-flow coupling, was imported into the model as a parameter [20].

3.2. Anand model

The Anand model is a unified viscoplastic constitutive equation proposed by Anand and Brown [21–23]. The model incorporates time-dependent creep (transient and steady-state), and time-independent plastic strain simultaneously generated during the deformation process. Two basic features of this model become immediately apparent. Firstly, no explicit yield conditions or loading/unloading criteria are required. Plastic strain is assumed wherever the stress is non-zero, although the plastic flow rate may be immeasurably small at low stress points. Second, the isotropic resistance to plastic flow, which depends on the internal state of the material, is represented by a single scalar. The behavior of highly deformed materials may be conveniently described by the unified constitutive equation. Large deformation also enables more direct matching of material parameters to experimental data.

3.2.1. Governing equations

In the Anand model, flows are expressed by

$$\dot{\varepsilon}_p = A\exp\left(-\frac{Q}{RT}\right)\left[\sinh\left(\xi\frac{\sigma}{s}\right)\right]^{1/m} \quad (1)$$

where $\dot{\varepsilon}_p$ is the inelastic strain rate, A is a pre-exponential factor, Q is the activation energy, R is the universal gas constant, and T is the temperature. The stress multiplier and equivalent stress in steady plastic flow are denoted by ξ and σ, respectively, s is the deformation resistance (in units of stress), and m is the strain rate sensitivity.

The internal variable $\dot{s}$ evolves as

$$\dot{s} = h(\sigma,s,T)\dot{\varepsilon}_p - \dot{r}(s,T) \quad (2)$$

The first term on the right-hand side of Eq. (2) is the strengthening function, given by

$$h(\sigma,s,T) = \left[h_0\left|1-\frac{s}{s^*}\right|^a \cdot \mathrm{sign}\left(1-\frac{s}{s^*}\right)\right]\cdot\dot{\varepsilon}_p, \quad a>1 \quad (3)$$

$$s^* = \hat{s}\left[\frac{\dot{\varepsilon}_p}{A}\exp\left(\frac{Q}{RT}\right)\right]^n \quad (4)$$

where h_0 is the hardening/softening constant, a is the strain rate sensitivity of hardening/softening, s^* denotes the saturation value of s for a given temperature and strain rate, n specifies the sensitivity of the strain rate to the saturation value of the deformation resistance, and $\hat{s}$ is a coefficient.

The second term on the right-hand side of Eq. (2) is the static recovery function, here set to zero.

Eqs. (1)–(4) are the basic equations of the Anand model. Collectively, they describe the characteristics of a material; namely, its temperature dependence, strain rate history and strain strengthening in all directions.

At a given temperature and strain rate, when the plastic deformation rate is proportional to loading strain rate, the material deformation reaches the steady plastic flowing state and the stress σ saturates at σ^*. Moreover, at a given temperature and loading stress, when the saturated stress in a viscoplastic material equals the loading stress, the plastic flow reaches steady state, and the deformation resistance s saturates at s^*.

In the Anand model, the steady-state plastic flow is given by

$$\dot{\varepsilon}_p = \dot{\varepsilon} = A\exp\left(-\frac{Q}{RT}\right)\left[\sinh\left(\xi\frac{\sigma^*}{s^*}\right)\right]^{1/m} \quad (5)$$

where $\dot{\varepsilon}$ is the loading strain rate.

From Eq. (4), the saturated stress σ^* is obtained as

$$\sigma^* = \frac{\hat{s}}{\xi}\left[\frac{\dot{\varepsilon}_p}{A}\exp\left(\frac{Q}{RT}\right)\right]^n \sinh^{-1}\left[\frac{\dot{\varepsilon}_p}{A}\exp\left(\frac{Q}{RT}\right)\right]^m \quad (6)$$

Isotropic hardening mechanisms such as dislocation density, solid solution hardening, and subgrain and grain size effects are encapsulated into a single internal variable in the Anand model, and the deformation resistance is proportional to the equivalent stress:

$$\sigma = cs, \quad c<1 \quad (7)$$

where c is a function of the strain rate and temperature, and is given by

$$c = \frac{1}{\xi}\sinh^{-1}\left[\left(\frac{\dot{\varepsilon}_p}{A}\exp(Q/RT)\right)^m\right] \quad (8)$$

Therefore, the stress in the Anand model can be written as

$$\sigma = \sigma^* - \left\{\left(\sigma^*-cs^*\right)^{1-a} + (a-1)\left[(ch_0)\left(\sigma^*\right)^{-a}\right]\varepsilon_p\right\}^{1/(1-a)} \quad (9)$$

According to the stress-strain curves at different temperatures and the strain rates obtained from hot compressive experiments, the ultimate strength σ_b can be assumed as the saturated stress when determining the steady stress. Consequently, the nine parameters of the Anand model, namely, Q, A, ξ, $\hat{s}$, m, n, a, h_0, and s_0, can be calculated by nonlinear least square fitting of the deformation law of 304 stainless steel at high temperature. The parameter values so obtained are listed in Table 3.

Table 3. Parameters of the Anand model

Q/(J·mol^{-1})	A/s^{-1}	ξ	$\hat{s}$/MPa	m	n	a	h_0/MPa	s_0/MPa
372555	2.0371×10^{14}	3.25	125.1	1.43	2.174	1.5	3093.1	35

3.2.2. Verification of the Anand model

To verify the applicability of the Anand model to the current work, the stress–strain curves of 304 stainless steel samples at 1250°C were simulated by ANSYS. The stress–strain curves are plotted in Fig. 2. The size of the model, taken from the axial cross section of the actual compressed sample, is 5 mm × 15 mm. The loading conditions were as follows: (i) the displacement on the left side of model is constrained and the displacement along the X axis is zero, i.e., $\partial U/\partial X = 0$, where U denotes displacement; (ii) the system is assumed symmetric about the X axis of the lower boundary, i.e., the displacement along the Y axis is zero; (iii) the displacement load of 7.5 mm towards the left is assigned at the nodes on the right side of the model. As

evidenced in Fig. 2, the simulated and measured stress–strain curves in the high temperature zone are highly consistent, confirming the reliability of the Anand model.

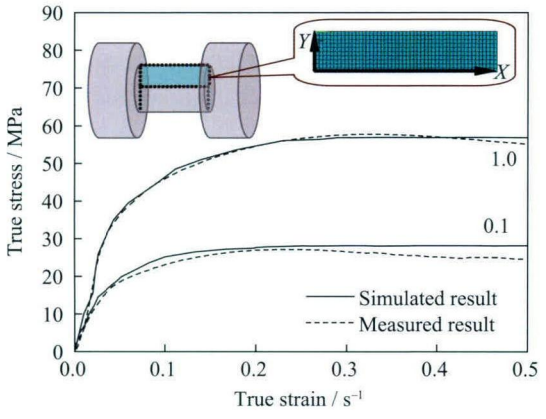

Fig. 2. Comparison between the simulated and measured stress–strain curves.

4. Results and analyses

4.1. Observation of cracks in the thin steel strip

Within the scope of the plate width, the surface of the thin steel strip was marked with cracks up to 100 mm length. The microscopic morphologies of the surface cracks are shown in Fig. 3. Larger cracks in Fig. 3(a) are nearly 100 μm wide. The cracks follow a tortuous rather than a straight path, and larger cracks typically branch into numerous micro-cracks. These defects mainly arise from nonuniform solidification of the strip surface [24], and are initiated at points of hysteretic solidification. Since the speed of cooling is nonuniform, the material shrinks inhomogeneously, resulting in local stress concentration. Cracking occurs when the local stress exceeds the ultimate strength of the material. Under mechanical stress, the cracks propagate and develop to form different morphologies. Detailed observation revealed that most of the cracks were transgranular (i.e., passed through the grain) (Fig. 3(b)), but a number of intergranular cracks were also present (Fig. 3(c)). Transgranular cracks usually develop under stress, while intergranular cracks, which destructively traverse the grains, are induced by external forces. Figs. 3(b) and 3(c) also reveal numerous spherical and strip-like inclusions (delineated by rectangles). From the EDS analysis, the inclusions were found to chiefly contain Mg, Al, Mn, Cr, Ca, and O. Thus, they are speculated to comprise complex oxides, such as MgO, Al_2O_3, MnO, Cr_2O_3, and CaO. Inclusions exist as independent phases in the steel, destroying the continuity of the matrix. Accordingly, they accelerate the formation and expansion of cracks when local stress is applied. Therefore, elucidating the stress distribution in thin steel strips during the twin-roll casting process is important for understanding how cracks form and extend, predicting their location, and preventing their occurrence.

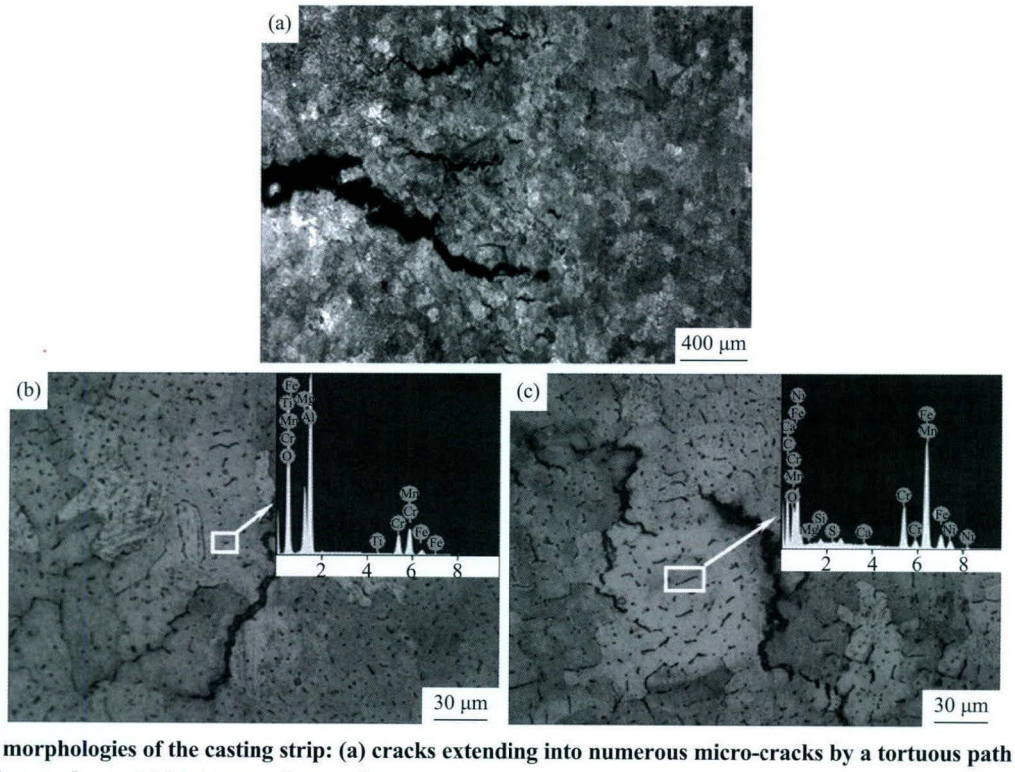

Fig. 3. Crack morphologies of the casting strip: (a) cracks extending into numerous micro-cracks by a tortuous path and branches, (b) transgranular cracks, and (c) intergranular cracks.

4.2. Simulation of stress fields in thin steel strips

Fig. 4 displays the simulated stress field in the molten pool. Higher stress concentrates chiefly at the exit and the roller contact positions. During twin-roll casting, the liquid in contact with the rollers dramatically cools under the action of cooling water, and a high-stress shell forms on the roller surface as the metal solidifies and is extruded by the rollers. The liquid at the exit solidifies because most of the heat is extracted by the rollers, generating large tensile stress. In Fig. 4(b), lines A, B, and C indicate the center line, the direction of thickness of the thin steel strip, and the strip-roller contact surface at the exit, respectively.

Fig. 5 shows the von Mises equivalent stress distributions of lines A, B and C in strips cast at different speeds. The overall stress along all three lines decreases with increasing casting speed. The largest stress along line A is localized near the edge (Fig. 5(a)), while along lines B and C it appears near the center (Fig. 5(b)) and the edge (Fig. 5(c)) of the strip, respectively.

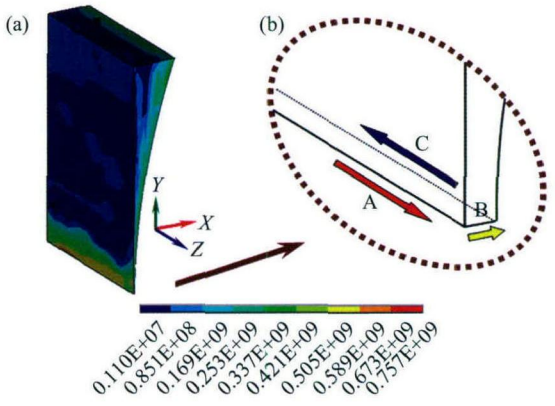

Fig. 4. Stress field of the molten pool (a) and an enlarged drawing of the exit (b).

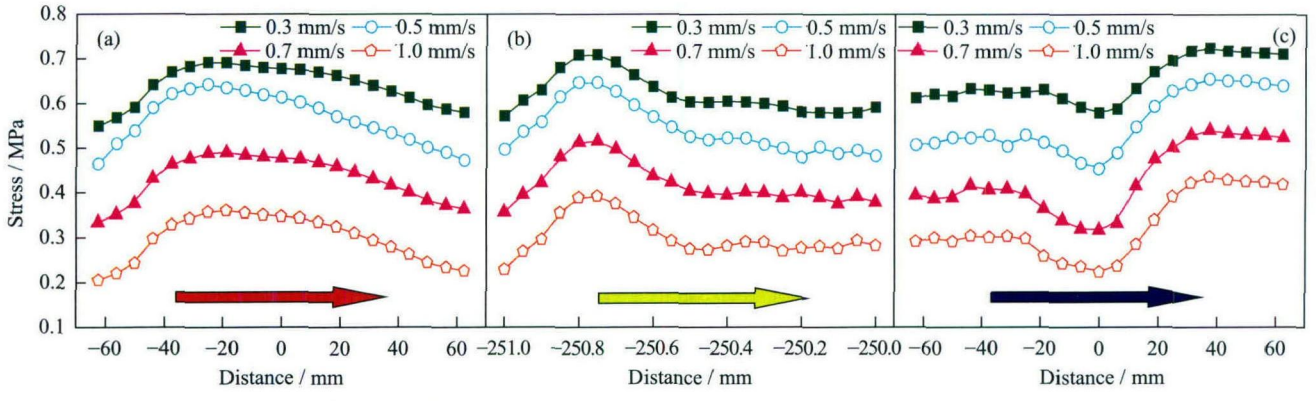

Fig. 5. Stress distributions of line A (a), line B (b), and line C (c) along the exit at different casting speeds.

Fig. 6 shows the von Mises equivalent stress distribution of lines A, B and C in strips cast at different pouring temperatures. Similar to casting speed, as the pouring temperature increased, the overall stress decreased along lines A, B, and C. Pouring temperature exerted no effect on the sites of maximum stress.

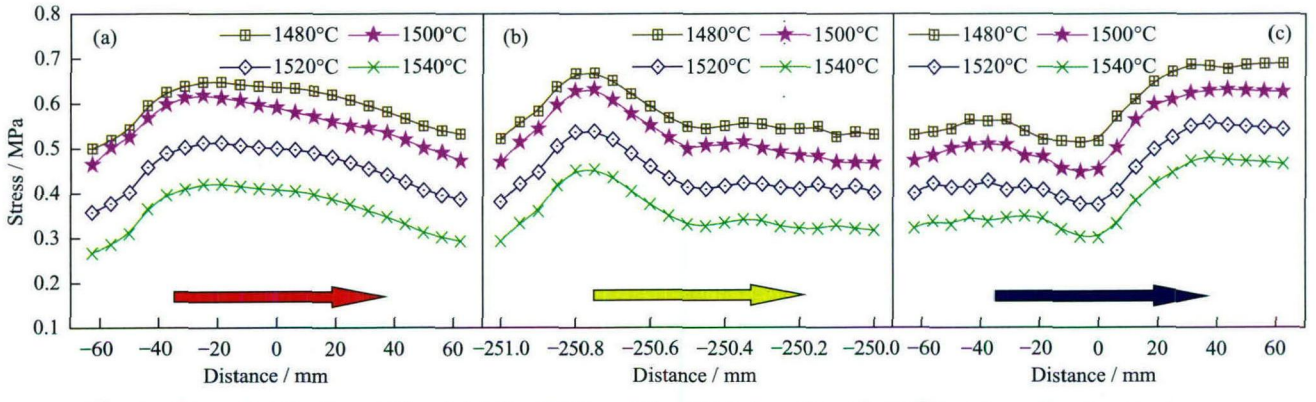

Fig. 6. Stress distributions of line A (a), line B (b), and line C (c) along the exit at different pouring temperatures.

4.3. Parameter optimization of twin-roll casting

Surface cracking has always been a problem in twin-roll casting technology. However, most research on strip cracking has focused on experimental evaluation. By applying continuous casting theory, we can optimize the technical

parameters to control the critical stress during the rolling process.

Ramacciotti [25] reported that cracks are generated on the casting block under extensive tensile stress in the transverse and longitudinal directions. He also proposed suspicious factor criteria for deciding whether cracks will appear, i.e., the casting blank surface remains crack-free if the suspicious factors are less than 1.

The suspicious factors of crack formation are defined as follows:

$$\text{T.C.I.} = [\sigma_X / \sigma_R]_{\max} \tag{10}$$

$$\text{L.C.I.} = [\sigma_z / \sigma_R]_{\max} \tag{11}$$

where T.C.I. and L.C.I are the suspicious factors of transverse and longitudinal cracking, respectively, σ_X and σ_Y are the simulated stress components along the X and Y axes, respectively, and σ_R is the critical stress, given by

$$\sigma_R = \kappa (T_{sol} - T)^q \tag{12}$$

where T_{sol} is the regular solidus temperature, T is the simulated temperature distribution, κ is a proportionality constant ($1.2^{-0.5}$ MPa·K$^{-0.5}$), and q is a constant (0.5).

The effects of casting speed and pouring temperature on the distribution of suspicious factors can now be discussed in detail.

4.3.1. Casting speed

Fig. 7 shows the transverse and longitudinal suspicious factor distributions of lines A and C at different casting speeds. To determine these distributions, the stress distributions were inserted into Eqs. (10) and (11). At casting speeds of 0.3 m/s and 0.5 m/s, most of the T.C.I. values along both lines exceed 1, indicating that transverse cracking will likely occur (see Figs. 7(a) and 7(b)). At 0.7 m/s, most of the T.C.I. values are constrained within 1. At the highest casting speed (1.0 mm/s), all values are below 1. At a casting speed of 0.5 m/s, most of the L.C.I. values exceed 1 along line A, but are typically below 1 along line C (see Figs. 7(c) and 7(d)). At casting speeds below 0.5 m/s, the L.C.I. values generally exceed 1 along both lines. By contrast, a casting speed of 0.7 m/s is sufficient to constrain all L.C.I. values of lines A and C within 1. In conclusion, the casting speed should be controlled above 0.7 m/s to ensure high strip quality.

4.3.2. Pouring temperature

Fig. 8 plots the transverse and longitudinal suspicious

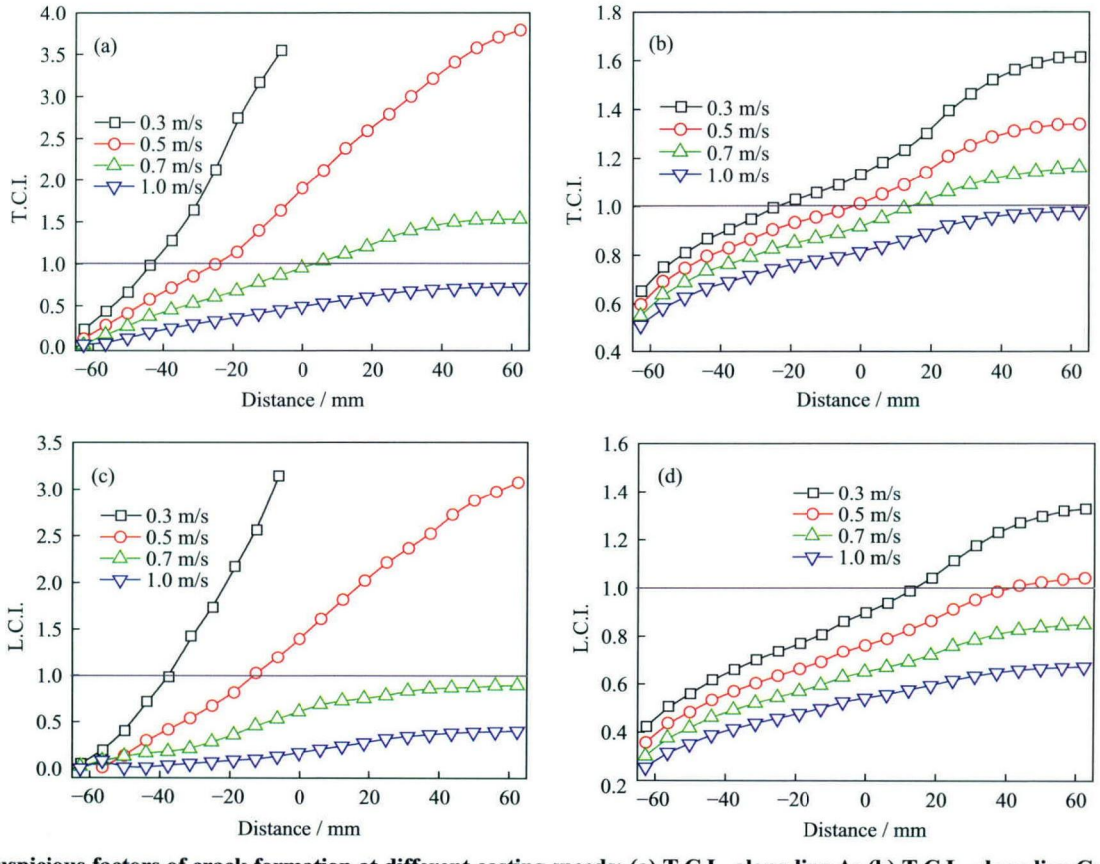

Fig. 7. Suspicious factors of crack formation at different casting speeds: (a) T.C.L. along line A; (b) T.C.L. along line C; (c) L.C.L. along line A; (d) L.C.L. along line C.

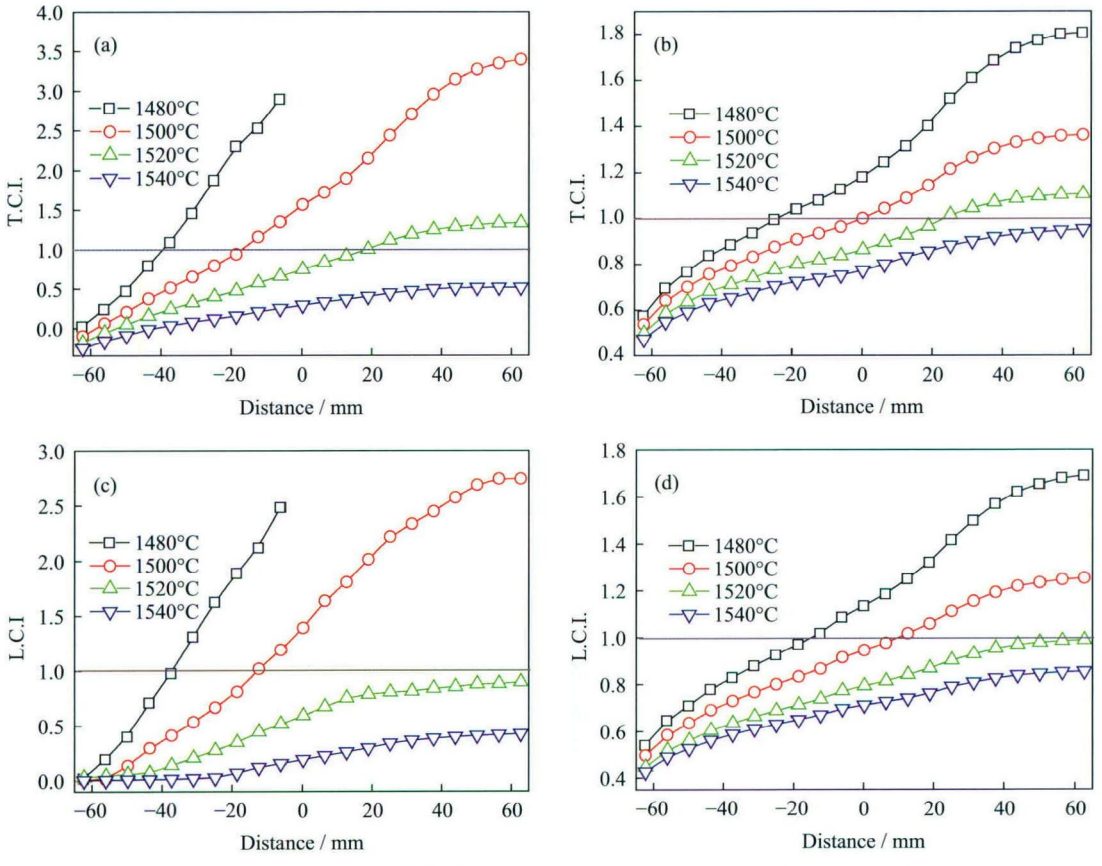

Fig. 8. Suspicious factors of crack formation at different pouring temperatures: (a) T.C.L. along line A; (b) T.C.L. along line C; (c) L.C.L. along line A; (d) L.C.L. along line C.

factor distributions of lines A and C at different pouring temperatures. At 1480 and 1500°C, most of the T.C.I. values exceed 1 along both lines (see Figs. 8(a) and 8(b)). The T.C.I values of both lines typically fall below 1 when the pouring temperature exceeds 1520°C. At a pouring temperature of 1540°C, all T.C.I. values of both lines are constrained within 1. The L.C.I. values along line A typically exceed 1 at 1500°C, whereas those along line C are chiefly below 1 at this temperature (see Figs. 8(c) and 8(d)). At pouring temperatures below 1500°C, the L.C.I. values along both directions are generally larger than 1, but at 1520°C, all L.C.I. values of both lines are constrained within 1. Therefore, the pouring temperature should be controlled above 1520°C to ensure high quality.

5. Discussion

Previously, we investigated the temperature field in stainless steel during twin-roll casting [8], and revealed that the position of the freezing point depends on both the roll gap (strip thickness) and roll radius. As the roll gap increases or the roll radius reduces, the position of the freezing point shifts toward the exit and the temperature at the exit of the strip increases, which encourages the steel break phenomenon. Thus, to prevent steel breakage, the freezing point should be elevated. Without altering the other conditions, reducing the pouring temperature will reduce the temperature of the whole molten pool, thereby raising the freezing point. Similarly, if the casting speed is reduced, more heat is extracted by the rollers, the temperature of the whole molten pool is reduced, and the freezing point consequently rises. That is, the critical pouring temperature and casting speed can be achieved by widening the roll gap and reducing the roller radius.

6. Conclusions

(1) Numerous cracks were formed on the surfaces of steel strips fabricated by twin-roll casting. The cracks followed a tortuous path and frequently forked into a multitude of micro-cracks. Further observation revealed both transgranular and intergranular cracks.

(2) Regions of high stress in the molten pool are the exit and roller contact positions. The overall stress at the exit de-

creased with increasing casting speed and pouring temperature.

(3) To preserve the integrity of the strips, the casting speed and pouring temperature should be controlled above 0.7 m/s and 1520°C, respectively.

Acknowledgements

The authors would like to express their gratitude for projects supported by Natural Science Foundation of Hebei Province, China (E2012203019).

References

[1] J.H. Bae, A.K.P. Rao, K.H. Kim, and N.J. Kim, Cladding of Mg alloy with Al by twin-roll casting, *Scripta Mater.*, 64(2011), No. 9, p. 836.

[2] S. Das, N.S. Lim, J.B. Seol, H.W. Kim, and C.G. Park, Effect of the rolling speed on microstructural and mechanical properties of aluminum–magnesium alloys prepared by twin roll casting, *Mater. Des.*, 31(2010), No. 3, p. 1633.

[3] H. Zhao, P.J. Li, and L.J. He, Kinetics of recrystallization for twin-roll casting AZ31 magnesium alloy during homogenization, *Int. J. Miner. Metall. Mater.*, 18(2011), No. 5, p. 570.

[4] Z.W. Chen, J. Zhao, and X.L. Hao, Microstructure and texture evolution of TRC A8006 alloy by homogenization, *Int. J Miner. Metall. Mater.*, 20(2013), No. 5, p. 433.

[5] L.L. Chang, J.H. Cho, and S.K. Kang, Microstructure and mechanical properties of twin roll cast AM31 magnesium alloy sheet processed by differential speed rolling, *Mater. Des.*, 34(2012), p. 746.

[6] S. Das, N.S. Lim, H.W. Kim, and C.G. Park, Effect of rolling speed on microstructure and age-hardening behaviour of Al–Mg–Si alloy produced by twin roll casting process, *Mater. Des.*, 32(2011), No. 8-9, p. 4603.

[7] B. Wang, J.Y. Zhang, X.M. Li, and W.H. Qi, Simulation of solidification microstructure in twin-roll casting strip, *Comput. Mater. Sci.*, 49(2010), Suppl., p. S135.

[8] Y. Fang, Z.M. Wang, Q.X. Yang, Y.K. Zhang, L.G. Liu, H.Y. Hu, and Y. Zhang, Numerical simulation of the temperature fields of stainless steel with different roller parameters during twin-roll strip casting, *Int. J. Miner. Metall. Mater.*, 16(2009), No. 3, p. 304.

[9] H. Zhao, P.J. Li, and L.J. He, Coupled analysis of temperature and flow during twin-roll casting of magnesium alloy strip, *J. Mater. Process. Technol.*, 211(2011), No. 6, p. 1197.

[10] Y.C. Miao, X.M. Zhang, H.S. Di, and G.D. Wang, Numerical simulation of the fluid flow, heat transfer, and solidification of twin-roll strip casting, *J. Mater. Process. Technol.*, 174(2006), No. 1-3, p. 7.

[11] X.M. Zhang, Z.Y. Jiang, L.M. Yang, X.H. Liu, G.D. Wang, and A.K. Tieu, Modelling of coupling flow and temperature fields in molten pool during twin–roll strip casting process, *J. Mater. Process. Technol.*, 187-188(2007), p. 339.

[12] J. Zeng, R. Koitzsch, H. Pfeifer, and B. Friedrich, Numerical simulation of the twin-roll casting process of magnesium alloy strip, *J. Mater. Process. Technol.*, 209(2009), No. 5, p. 2321.

[13] A. Hadadzadeh and M.A. Wells, Mathematical modeling of thermo-mechanical behavior of strip during twin roll casting of an AZ31 magnesium alloy, *J. Magnesium Alloys*, 1(2013), No. 2, p. 101.

[14] S. Amit and S. Yogeshwar. Modeling of thermo-mechanical stresses in twin-roll casting of aluminum alloys, *Mater. Trans.*, 43(2002), No. 2, p. 214.

[15] M. Gupta and Y. Sahai, Mathematical modeling of thermally induced stresses in two-roll melt drag thin strip casting of steel, *ISIJ Int.*, 40(2000), No. 2, p. 137.

[16] P. Zhang, Y.K. Zhang, L.G. Liu, X.J. Ren, Y. Zhang, Y. Fang, and Q.X. Yang, Numerical simulation on the stress field of austenite stainless steel during twin-roll strip casting process, *Comput. Mater. Sci.*, 52(2012), No. 1, p. 61.

[17] D.J. Yu, X. Chen, G. Chen, G.Q. Lu, and Z.Q. Wang, Applying Anand model to low-temperature sintered nanoscale silver paste chip attachment, *Mater. Des.*, 30(2009), No. 10, p. 4574.

[18] L.G. Liu, Q. Li, B. Liao, Y.K. Gao, Y.H. Wang, X.J. Ren, and Q.X. Yang, Stress–strain behaviors simulation of high chromium steel at elevated temperatures, *J. Mater. Eng. Perform.*, 19(2010), No. 7, p. 921.

[19] X.D. Hu and D.Y. Ju, Application of Anand's constitutive model on twin roll casting process of AZ31 magnesium alloy, *Trans. Nonferrous Met. Soc. China*, 16(2006), Suppl. 1, p. s586.

[20] L.L. Liu, B. Liao, J. Guo, L.G. Liu, H.Y Hu, Y. Fang, and Q.X. Yang, 3D numerical simulation on thermal flow coupling field of stainless steel during twin-roll casting, *J. Mater. Eng. Perform.*, 23(2014), p. 39.

[21] S.B. Brown, K.H. Kim, and L. Anand, An internal variable constitutive model for hot working of metals, *Int. J. Plast.*, 5(1989), No. 2, p. 95.

[22] A.M. Lush, G. Weber, and L. Anand, An implicit time-integration procedure for a set of internal variable constitutive equations for isotropic elasto-viscoplasticity, *Int. J. Plast.*, 5(1989), No. 5, p. 521.

[23] G.G. Weber, A.M. Lush, A. Zavaliangos, and L. Anand, An objective time-integration procedure for isotropic rate-independent and rate-dependent elastic–plastic constitutive equations, *Int. J. Plast.*, 6(1990), No. 6, p. 701.

[24] B. Forbord, B. Andersson, F. Ingvaldsen, O. Austevik, J.A. Horst, and I. Skauvik, The formation of surface segregates during twin roll casting of aluminium alloys, *Mater. Sci. Eng. A*, 415(2006), No. 1-2, p. 12.

[25] A. Ramacciotti, Thermo-mechanical behavior of the solidified shell in a "funnel-shaped" mold for continuous casting of thin slabs, *Steel Res.*, 59(1988), p. 438.